Journal of Physics Communications

PAPER

Blue-noise sampling for human retinal cone spatial distribution modeling

Matteo Paolo Lanaro[1,3] (ORCID), **Hélène Perrier**[2], **David Coeurjolly**[2], **Victor Ostromoukhov**[2] **and Alessandro Rizzi**[1]

1   Università degli Studi di milano, Via Celoria, 18 20133, Milano, Italy
2   Université de Lyon, 43 Bd 11 novembre 1918, F-69622, Villeurbanne, France
3   Author to whom any correspondence should be addressed.

E-mail: matteo.lanaro@unimi.it, helene.perrier@liris.cnrs.fr, david.coeurjolly@liris.cnrs.fr, victor.ostromoukhov@liris.cnrs.fr and alessandro.rizzi@unimi.it

Abstract

This paper proposes a novel method for modeling retinal cone distribution in humans. It is based on Blue-noise sampling algorithms being strongly related with the mosaic sampling performed by cone photoreceptors in the human retina. Here we present the method together with a series of examples of various real retinal patches. The same samples have also been created with alternative algorithms and compared with plots of the center of the inner segments of cone photoreceptors from imaged retinas. Results are evaluated with different distance measure used in the field, like nearest-neighbor analysis and pair correlation function. The proposed method can effectively describe features of a human retinal cone distribution by allowing to create samples similar to the available data. For this reason, we believe that the proposed algorithm may be a promising solution when modeling local patches of retina.

1. Introduction

Sampling is the reduction of a continuous signal into a discrete one, or the selection of a subset from a discrete set of signals. For sampling to be effective, samples should be uniformly distributed in a way that there are no discontinuities; but at the same time, regular repeating patterns should be avoided, to prevent aliasing. In the human retina, the mosaic of the cone photoreceptor cells samples the retinal optical projection of the scene, achieving the first neural coding of the spectral information from the light that enters the eye. To solve the sampling problem, the human retina has adopted an arrangement of photoreceptors that is neither perfectly regular nor perfectly random. Local analysis of foveal mosaics shows that cones are arranged in hexagonal or triangular clusters, however, when this analysis is extended to larger areas, cones are organized into particular patterns, such as parallel curving and circular rows, which are generally associated with rotated local clusters.

There are different theories regarding the regularity and development of the cone cells mosaic. Wassle and Riemann [1] proposed two models based on mechanisms that assume the self-regulation of an original random pattern, one with a repulsive force acting between nerve cells and the other based on competition for territory for each neighboring cell. Later, Yellott [2] discovered that the photoreceptors in the human retina, especially the cones, are distributed conforming to a Poisson disk distribution. He performed spectral analysis to an array of cones treated as sampling points and observed that the spectral properties of cones mosaic are representative of a Poisson disk array, with the additional restriction of a minimum distance between the center of the cells and their nearest neighbors, because of the size of the cells. This was confirmed by Galli-Resta *et al*, which investigated the spatial features of the ground squirrel retinal mosaics, suggesting that a minimal-spacing rule d_{min} in conjunction with an adequate density of receptors can adequately describe the array of rods and S cones [3]. Poisson disk distribution is now regarded as one of the best sampling patterns, by virtue of its blue-noise power spectrum [4]. In Figure 1 (a-f) are presented some examples of different 2-D samplers.

It is still unclear how the spatial distribution and mean density of cones can affect the sampling of a retinal image [5]. An interesting evidence of this open issue is the experiment reported by Hofer *et al* [6], who tested the

perception of stimuli of small spatial scale. Showing brief, monochromatic flashes of light of half the diameter of a cone size on previously characterized retinal areas of the subjects, authors described the same stimuli with a large number of hue categories, including white, blue and purple, indicating that the stimulation of two different cones with the same photopigment results in different color sensations, even with no stimuli in different regions of the retina or on other wavelength-sensitive cones.

In this study, we examined the Nearest Neigbour (NN) regularity index of the population of cones in images of real human retina. We then compared the results to another measure of spatial patterning, the Pair Correlation Function. The goal of this paper is to show that the sampling properties of the cone photoreceptor mosaic can be modeled by a blue-noise algorithm, and that they can be used to generate sampling arrays characterized by the same features of the retinal cone mosaics. More specifically, we want to identify an algorithm capable of generating sampling arrays with the same range of densities in the retina, and use specific metrics to compare the spatial and spectral properties of the cones distribution.

2. Related works

2.1. Retinal and Cone sampling modeling

In the past two decades, interesting research works on retinal modeling focus on neural behavior [7–9]; as an example, *Virtual Retina* by Wohrer and Kornprobst is a large scale simulation software that transforms a video input into spike trains, designed with a focus on nonlinearities and implementing a contrast gain control mechanism.

However, there have not been many attempts to model the cone sampling array. As far as we are aware, the first state-of-the-art sampling model for positioning cones in the retina mimicking qualities of the human sampling was described by Ahumada [10]. It uses cones, surrounded by circular disks representing their region of influence, and places them starting from the center of the retina, applying a random jitter to each point. There is also an attempt at generating a space-varying parameter model, to extend the modeling capabilities past the foveola, by varying with eccentricity the mean radius of the cone disk, the standard deviation of the cone disk radius, and the standard deviation of postpacking jitter; but ultimately those parameters seem to be only fit for the foveola.

After their studies on human photoreceptor topography, Curcio and Sloan continued in Ahumada's direction proposing a model of cones distribution based on regular arrays subjected to a spatial compression and a jitter, to fit the actual cones mosaic [11]. Their analysis was based on the distribution of distance and angles of neighboring cones, comparing real mosaics with artificially generated ones, and evidencing anisotropies in retinal cell spacing.
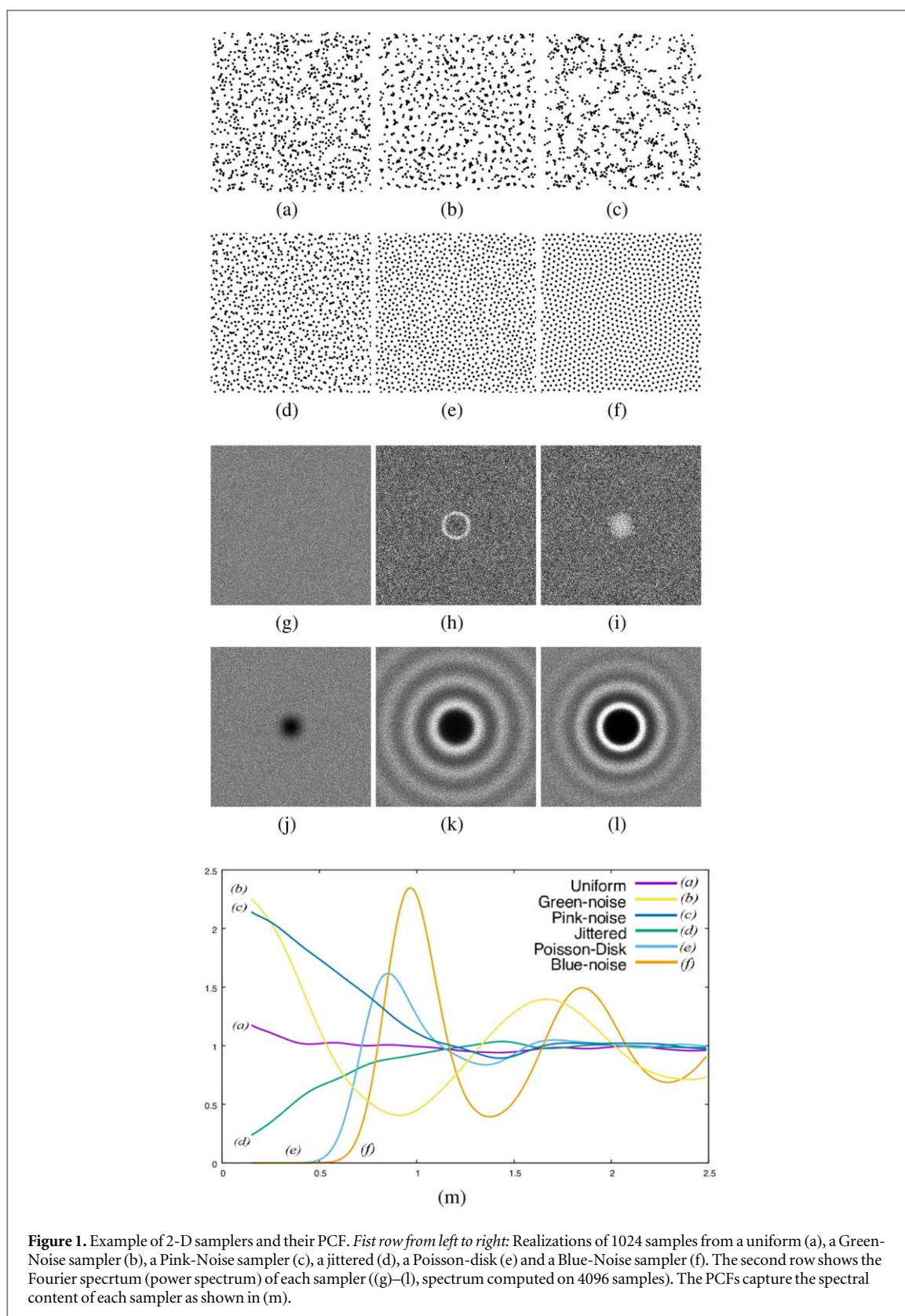
Another attempt at modeling the sampling properties of the cone mosaic was proposed by Wang [12], which created a polar arranged array of cones and jittered the points according to the standard deviation of a Gaussian distribution, constrained by a minimal spacing rule. The comparison of power spectrum of the human foveal cones and the generated sampling arrays show similarities, and the generated arrays exhibit some basic features of the mosaic of foveal cones.

In Deering's [13] human eye model, cones are modeled individually as a center points surrounded by points that define a polygon constituting the boundaries of the cell, each photoreceptor is then subjected to attractive and repulsing forces to adjust its position. This retinal synthesizer is then validated by calculating the neighbor fraction ratio and by empirically measuring the cone density in cells/mm^2 and comparing it from data from Curcio *et al* [14].

2.2. Blue noise distributions

Coined by Ulichney [15], the term *blue noise* refers to an even, isotropic, yet unstructured distribution of points. Blue noise was first recognized as crucial in dithering of images since it captures the intensity of an image through its local point density, without introducing artificial structures of its own. It rapidly became prevalent in various scientific fields, especially in computer graphics, where its isotropic properties lead to high-quality sampling of multidimensional signals, and its absence of structure prevents aliasing. It has even been argued that its visual efficacy (used to some extent in stippling and pointillism) is linked to the presence of a blue-noise arrangement of photoreceptors in the retina discovered by Yellott [2]. Over the years, a variety of research efforts targeting both the characteristics and the generation of blue noise distributions have been conducted in computer graphics.

Arguably the oldest approach to algorithmically generate point distributions with a good balance between density control and spatial irregularity is through error diffusion [15, 16], which is particularly well adapted to low-level hardware implementation in printers. Concurrently, a keen interest in uniform, regularity-free distributions appeared in computer rendering in the context of anti-aliasing [17]. Cook [18] proposed the first

Figure 1. Example of 2-D samplers and their PCF. *Fist row from left to right:* Realizations of 1024 samples from a uniform (a), a Green-Noise sampler (b), a Pink-Noise sampler (c), a jittered (d), a Poisson-disk (e) and a Blue-Noise sampler (f). The second row shows the Fourier specrtum (power spectrum) of each sampler ((g)–(l), spectrum computed on 4096 samples). The PCFs capture the spectral content of each sampler as shown in (m).

dart-throwing algorithm to create Poisson disk distributions, for which no two points are closer together than a certain threshold. Considerable efforts followed to modify and improve this original algorithm [19–23]. Today's best Poisson disk algorithms are very efficient and versatile [24, 25], even running on GPUs [26–28].

Thanks to the pioneering work by Dippé and Wold [29], Mitchell [30], Cook [18], Shirley [31], the computer graphics community became sensitive to the fact that noise and aliasing are tightly coupled to sampling. A large variety of optimization-based approaches has been proposed since then. Two main optimization-based approaches have been developed and presented in numerous papers: (1) on-line optimization [20, 27, 24,

Table 1. μ, σ and regularity indexes of retinal mosaics. GN = Green Noise, PN = Pink Noise, BNOT = Blue Noise through Optimal Transport.

Data	μ	σ	RI
7-A	4.03456374	0.50612555	7.971 468 099
7-B	9.04250728	1.06718420	8.473 239 435
5	12.73315988	1.44799613	8.793 642 161
4–6	7.22426840	0.79458918	9.091 828 225
4–4	3.83590555	0.41681003	9.203 006 761
8-G	1.50767654	0.15854224	9.509 620 334
1-G	8.58240715	0.88831701	9.661 423 858
4–5	6.00671254	0.61540511	9.760 582 792
3-B	1.97490585	0.20006784	9.871 180 871
3-F	5.05986062	0.51204539	9.881 664 061
3-A	2.14670807	0.20446813	10.498 985 71
6	4.59784100	0.42302628	10.868 925 11
1-F	6.82704837	0.62173280	10.980 679 1
1-A	3.93220536	0.35599814	11.045 578 35
3-C	1.46598239	0.12902791	11.361 746 22
2-A	5.05899348	0.43416187	11.652 321
8-J	1.63116540	0.13651109	11.948 958 88
8-I	1.63433522	0.13589955	12.026 053 02
8-K	1.85141910	0.15104864	12.257 105 34
GN_512	0.01656738	0.01266479	1.308 143 909
GN_1024	0.01213441	0.00876178	1.384 925 079
PN_512	0.01873769	0.01319843	1.419 690 795
PN_1024	0.01340864	0.00933317	1.436 664 256
BNOT_1050	0.02969981	0.00138443	21.452 712 05
BNOT_2050	0.02132946	0.00093060	22.919 909 97
BNOT_4050	0.01514123	0.00064959	23.308 644 05

Table 2. l_∞ distances between pairs of PCFs. If this difference is under 0.1, the two distribution can be considered to be the same. It is clearly visible that the Dart Throwing and BNOT samplers are the closest from the measured distribution.

Data	BNOT 1024	DT 1024	Jitter 1024
1-A	0.507644	0.525371	0.945 527
1-F	0.52156	0.566554	0.912 223
1-G	0.778872	0.309411	0.663 769
2-A	0.298435	0.764314	1.134 42
3-A	0.408852	0.851508	1.1428
3-B	0.549172	0.518775	0.886 055
3-C	0.484184	0.597551	0.948 338
3-D	0.401644	1.1555	1.417 47
3-F	0.856925	0.484083	0.633 278
4-4	0.472629	0.598528	0.959 664
4-5	0.917283	0.262972	0.597 261
4-6	0.642895	0.525127	0.806 347
5	0.920215	0.383484	0.578 448
6	0.264755	0.809063	1.1713
7-A	0.778203	0.248315	0.761 941
7-B	0.803054	0.245291	0.686 117
8-G	0.826069	0.331142	0.638 697
8-I	0.301428	0.768822	1.133 56
8-J	0.297661	0.797065	1.146 51
8-K	0.327341	0.737896	1.106 08

32–43], and (2) off-line optimization [44–49], where the near-optimal solution is prepared in form of lookup tables, used in runtime. The present work uses the approach developed by de Goes *et al* [39], called *Blue Noise Through Optimal Transport* (BNOT), as reference. The reason behind our choice is that BNOT is the present best performing method among those trying to reproduce Blue Noise distributions.

In an effort to allow fast blue noise generation, the idea of using patterns computed offline was raised in [29]. To remove potential aliasing artifacts due to repeated patterns, Cohen *et al* [50] recommended the use of non-periodic Wang tiles, which subsequently led to improved hierarchical sampling [45] and a series of other tile-based alternatives [44, 46, 51, 52]. Wachtel *et al* [47] propose a tile-based method that incorporates spectral control over sample distributions. More recently, Ahmed *et al* [49] proposed a 2-D square tile-based sampling method with one sample per tile and controllable Fourier spectra. However, all precalculated structures used in this family of approaches rely on the offline generation of high-quality blue noise.

3. Methods

The cone mosaics used for this work are from previously published images of patches of real human retinas, as shown in the leftmost boxes of figures 2 through 6; they were acquired from the pdf versions of the papers or html, if available, and saved as png images. The pictures are from different subjects of various ages and were obtained with different techniques, ranging from histological techniques, where sample tissues are depicted with electronic microscopic imaging [14, 53–55], to more recent *in vivo* imaging techniques, which exploit adaptive optics like deformable mirrors coupled with a wavefront sensor to compensate for the ocular aberrations of the eye [56–59]. The *x* and *y* coordinates of the cells inner segments were manually plotted using WebPlotDigitizer [60]. This preliminary work has been based on a relatively small dataset sue to the difficulty of finding wide collections of retinal images. We understand these difficulties related also with problem of the use of different imaging techniques and tissue preparation and we hope to have larger datasets in the future. When analyzing the points distribution, the distance between the cone centers was converted in real μm on the retina by multiplying them with the appropriate scale factor of the image, determined by the size of the sample window's side. Conversion from degrees was performed according to the model from [61], with one degree of visual angle equal to 288 μm on the retina. Cone spacing values are compatible with Wyszecki and Styles [62], with the exception of the data from [55] exhibiting lower values, probably due to post mortem shrinkage. It is worth noting that the last retina from figure 4 and retinas from figure 5 have been cropped during analysis because they didn't fully fill the sampling window, and would have included uncharacterized areas.

3.1. Analysis of point process

In this section, we briefly introduce basic notions from Stochastic Point Processes [63]. A point process $\mathscr{S}$ is a stochastic generating point in a given domain Ω (here, $[0,1)^s$). We denote by $P_n := \{\mathbf{x}^{(1)}, \mathbf{x}^{(2)}, \cdots, \mathbf{x}^{(n)}\} \subset \Omega$ a realization of a point process with n samples. A point process $\mathscr{S}$ is *stationary* if it is invariant by translation, and isotropic if it is invariant by rotation. More formally, if we assume $\mathbf{P}$ a *probability measure*, $\mathscr{S}$ is stationary if $\forall\, \mathbf{x} \in \mathbb{R}^s$

$$\mathbf{P}(\mathscr{S}(\Omega)) = \mathbf{P}(\mathscr{S}(\Omega - \mathbf{x})), \tag{1}$$

and *isotropic* if any rotation or translation of $\mathscr{S}$ have the same statistical properties. We also define the *density* of a point set as the average number of samples inside a region B of volume V_B around a sample $\mathbf{x}$.
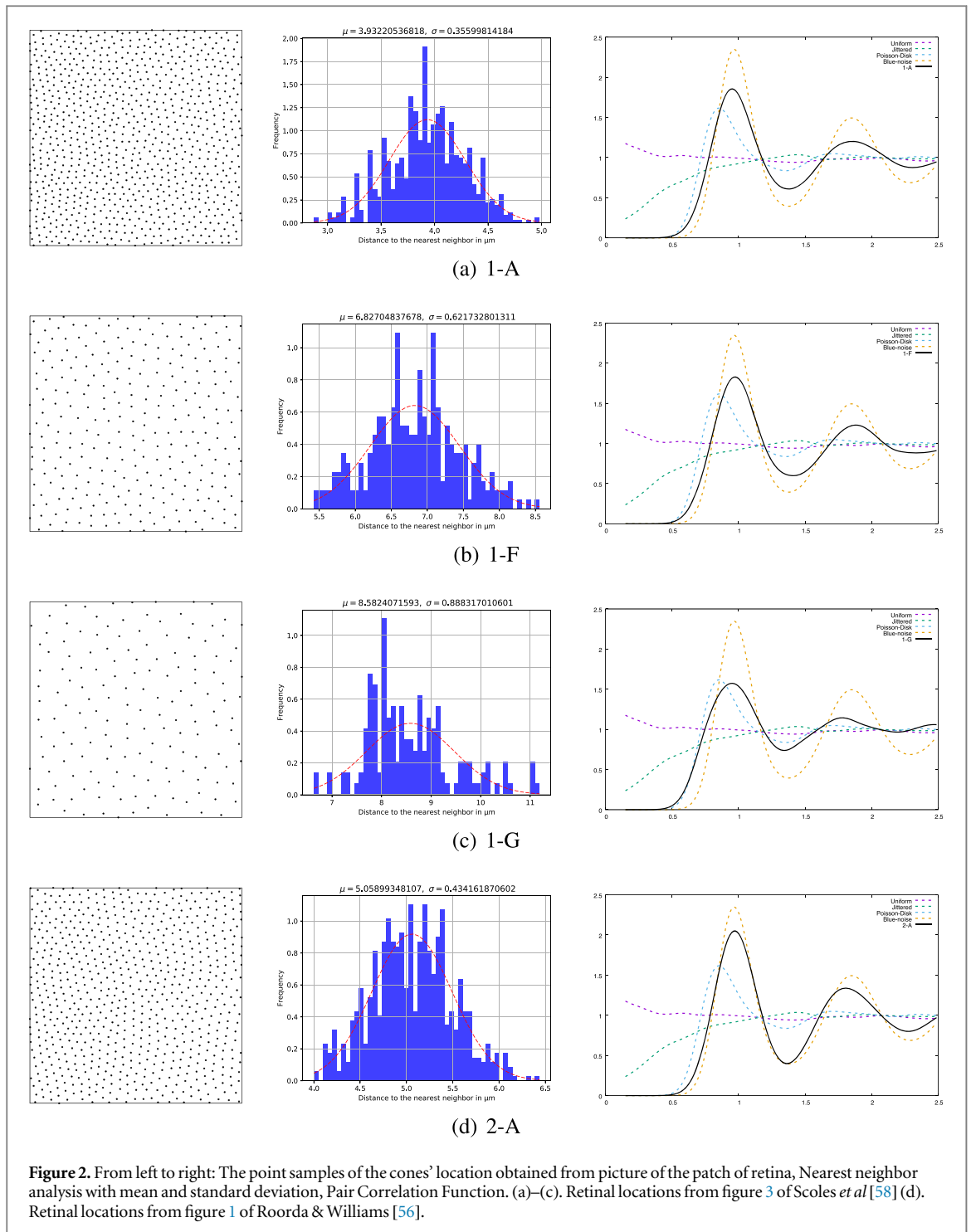
$$\lambda(x) := \frac{B(x)}{V_B}. \tag{2}$$

This density is constant for isotropic and stationary point processes. A sampler generating sets with a non constant density is sometimes called a *non-uniform* sampler. To characterize isotropic stationary point processes, the *Pair Correlation Function* (PCF) is a widely used tool. Such function is a characterization of the distribution of pair distances of a point process. Oztireli [41] devised a simplified estimator for this measure in the particular case of isotropic and stationary point processes. The PCF of a pointset P_n in the unit domain $[0, 1)^s$ is given by

$$\rho(r) = \frac{1}{n^2 r^{s-1}} \sum_{i \neq j} k_\sigma(r - d(\mathbf{x}^{(i)}, \mathbf{x}^{(j)})), \tag{3}$$

where $d(\mathbf{x}^{(i)}, \mathbf{x}^{(j)})$ is a distance measure between $\mathbf{x}^{(i)}$ and $\mathbf{x}^{(j)}$. The factor k_σ is used to smooth out the function. Oztireli relies on this smoothing to assume ergodicity for all sets. He uses the Gaussian function as a smoothing kernel, but one could use a box kernel or a triangle kernel instead. To compute a PCF, we use this estimator with 3 parameters, the minimal r, r_{min}, the maximal r, r_{max} and the smoothing value σ. Those values are usually chosen empirically. Note that as the number of samples increase, the distances between samples becomes very different for similar distributions. To reduce this effect, we normalize the distances in our estimations using the maximum radius for n samples ([64], equation (5)).

In figure 1, we illustrate how the PCF of several point processes captures the spectral content of the point distribution: a pure uniform sampling, Green-Noise and Pink-Noise samplers obtained using [52], a jittered

Figure 2. From left to right: The point samples of the cones' location obtained from picture of the patch of retina, Nearest neighbor analysis with mean and standard deviation, Pair Correlation Function. (a)–(c). Retinal locations from figure 3 of Scoles *et al* [58] (d). Retinal locations from figure 1 of Roorda & Williams [56].

sampler (for *N* samples, subdivision of the domain into regular $\sqrt{N} \times \sqrt{N}$ square tile and a uniform random sample is drawn in each tile), a Poisson-Disk sampler [22] and a Blue-noise sampler (BNOT) [39].

4. Results and discussion

The *regularity index*, or *conformity ratio* is a quantitative method used for assessing spatial regularity of photoreceptor distributions [1, 65, 66]. Spatial regularity in local patches is computed by numerically expressing the concentration of the nearest neighbor distances, that is by computing the inverse of the coefficient of variation (CV, also called coefficient of dispersion) of the distribution of nearest neighbor distances. Obviously, the highest/lower the CV (dispersion) of local neighborhoods sizes, the lowest/highest is the regularity index. In detail, to compute the regularity index, a k-d tree structure has been used to find the nearest-neighbor for each point, the distances between nearest neighbors are computed through the euclidean norm, and the distribution
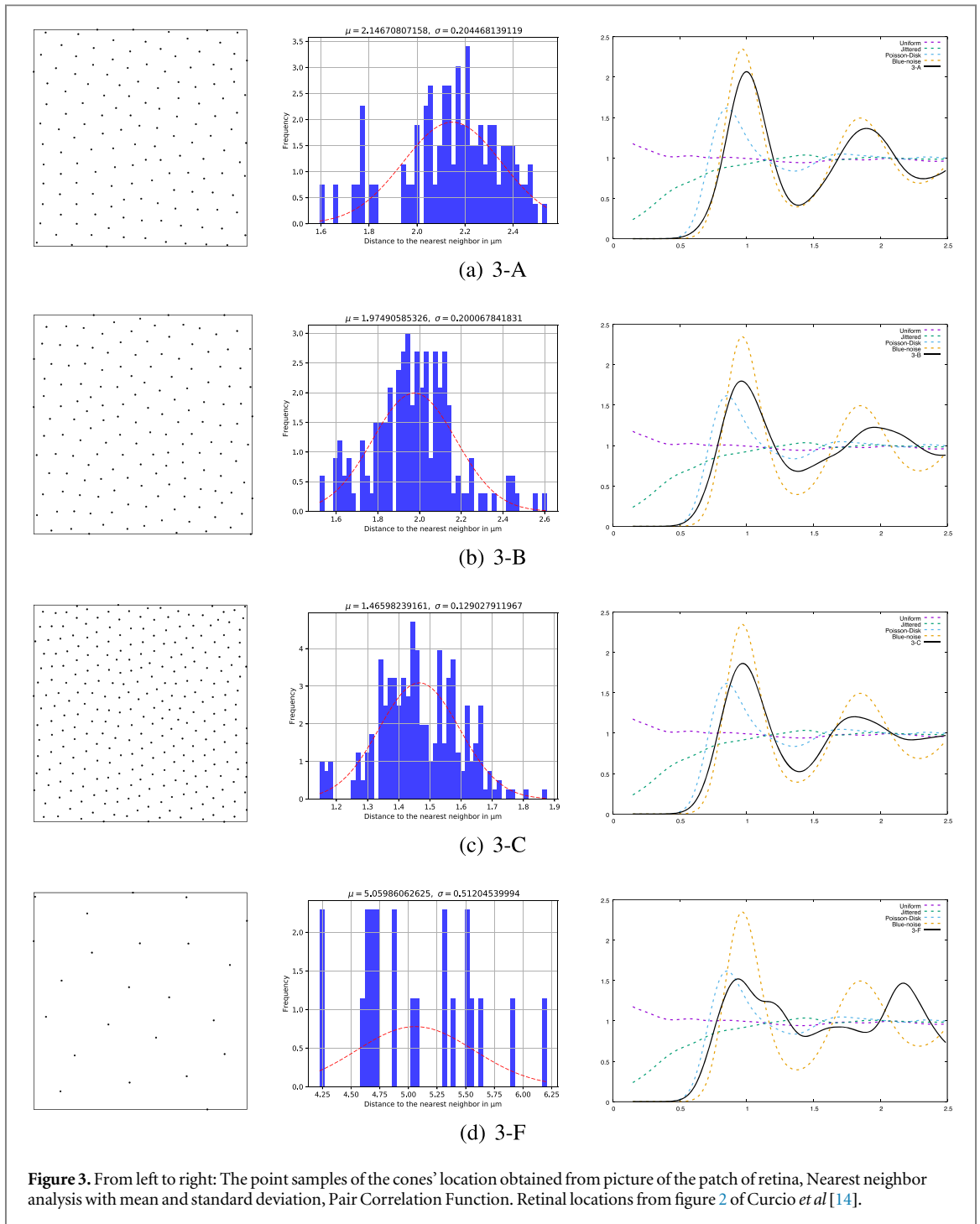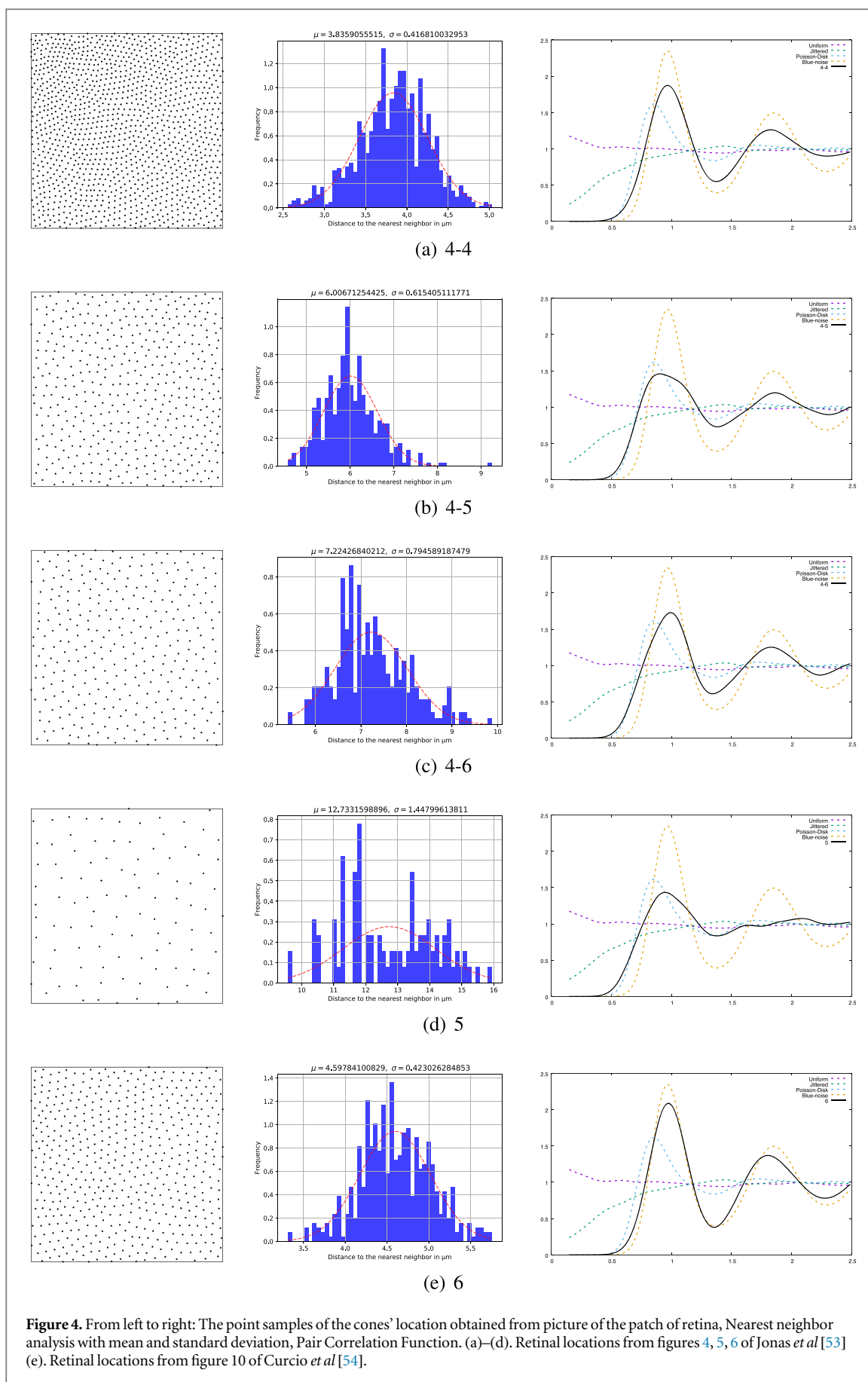
(a) 3-A

(b) 3-B

(c) 3-C

(d) 3-F

Figure 3. From left to right: The point samples of the cones' location obtained from picture of the patch of retina, Nearest neighbor analysis with mean and standard deviation, Pair Correlation Function. Retinal locations from figure 2 of Curcio *et al* [14].
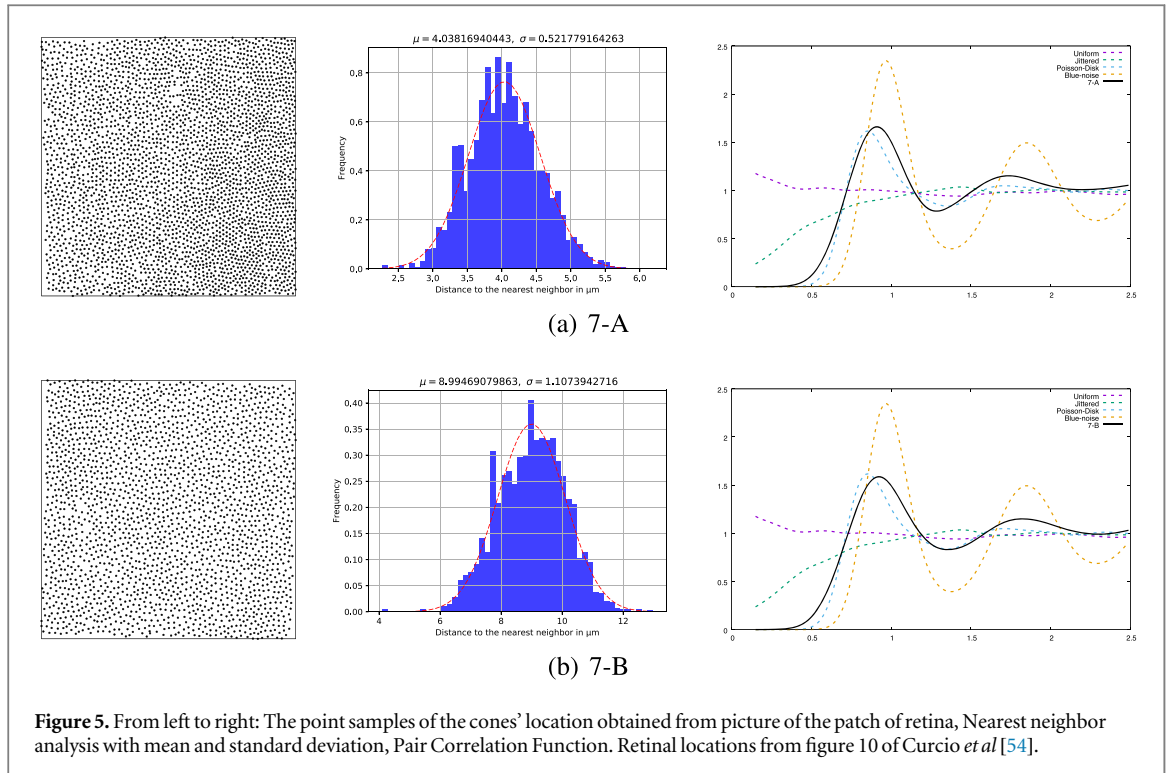
of all the computed nearest-neighbor distances is visualized through the normalized histogram. Each distribution of nearest-neighbours can be described by a normal Gaussian distribution described by the equation

$$P(x) = \frac{1}{\sigma\sqrt{2\pi}}e^{-(x-\mu)^2/2\sigma^2}. \tag{4}$$

where μ is the mean of the distribution and σ the standard deviation of the measurements. The regularity index is therefore expressed by the ratio of the mean μ by the standard deviation σ. This index is reported to be 1.9 for a full random sampling, where the standard deviation is higher. Anyhow, as mentioned above, the more regular the arrangement, the higher the value of the conformity index, usually 3–8 for retinal mosaics.

Regularity indexes for retinal data are shown in table 1. In contrast with previous claims, our calculated indexes range from 8 to 12. In the lower bound we show data obtained from [54], which instead of a retinal image shows the marked locations of the inner segments of photoreceptors; meanwhile in the upper bound,

Figure 4. From left to right: The point samples of the cones' location obtained from picture of the patch of retina, Nearest neighbor analysis with mean and standard deviation, Pair Correlation Function. (a)–(d). Retinal locations from figures 4, 5, 6 of Jonas *et al* [53] (e). Retinal locations from figure 10 of Curcio *et al* [54].

Figure 5. From left to right: The point samples of the cones' location obtained from picture of the patch of retina, Nearest neighbor analysis with mean and standard deviation, Pair Correlation Function. Retinal locations from figure 10 of Curcio *et al* [54].

close to 12, most of the data is from foveal centers in [55], with the exception of retina 8-G, where the different sizes of the photoreceptor profiles reflect different levels of sectioning through the inner segments.

The indexes for data generated with Green noise, Pink noise and BNOT samplers are presented in the same table. As expected, the indexes for Green and Pink noise, which, on average, equal 1.3 and 1.4 respectively, are lower than those that would have been obtained by a full random sampling; on the other side, for the BNOT data, the indexes values are much higher, more than two times of the highest values for retinal RIs. It is not very surprising that, thanks to the the uniformity optimization of BNOT, the indexes are so high; however, they are anyway distant from the infinite RI of regular lattices. Given the fact that fully regular hexagonal or square patterns are proven to have poor sampling properties and are therefore not suitable for simulating cone distributions, we believe that, for what regards the scope of this paper, a higher RI indicates that BNOT is better at generating point processes than the other analyzed point samplers.

A more recent and reliable method for assessing the goodness of these processes is the previously mentioned Pair Correlation Function (PCF). In table 2, we present the l_∞ distance, between our generated point sets and the measured PCF. From two PCFs ρ and ρ_2, we denote their l_∞ distance as the maximal distance between the two functions:

$$l_\infty(\rho, \rho_2) = \max_r |\rho(r) - \rho_2(r)|,$$ (5)

where r is a given radius. We rely on this measure as it was already used in [41] to compare PCFs, and we consider two PCFs similar if l_∞ is less than 0.1. Using such evaluation measure, the closest results are obtained when comparing BNOT to Dart Throwing samplers. Moreover, the higher the measured RI for the retinal distribution of photoreceptors, the lower the distance from BNOT PCF. The opposite happens when comparing retinal data with Dart throwing algorithm, the closer to the reported RI of 8, the lower the l_∞ distance. This evidences that not only the indexes are actually higher than the ones previously measured, but also that the most effective method to simulate these distributions comes from Blue-noise samplers.

5. Conclusions

Blue noise sampling can describe features of a human retinal cone distribution with a certain degree of similarity to the available data and can be efficiently used for modeling local patches of retina. We hope this work can be useful to understand how spatial distribution affects the sampling of a retinal image, or the mechanisms underlying the development of this singular distribution of neuron cells and the implications it has on human vision. Given the nature of blue-noise algorithms, it should be possible to develop an adaptive sampling model that spans the whole retina. However, there would be issues in validating the cone sampling, since imaging of the
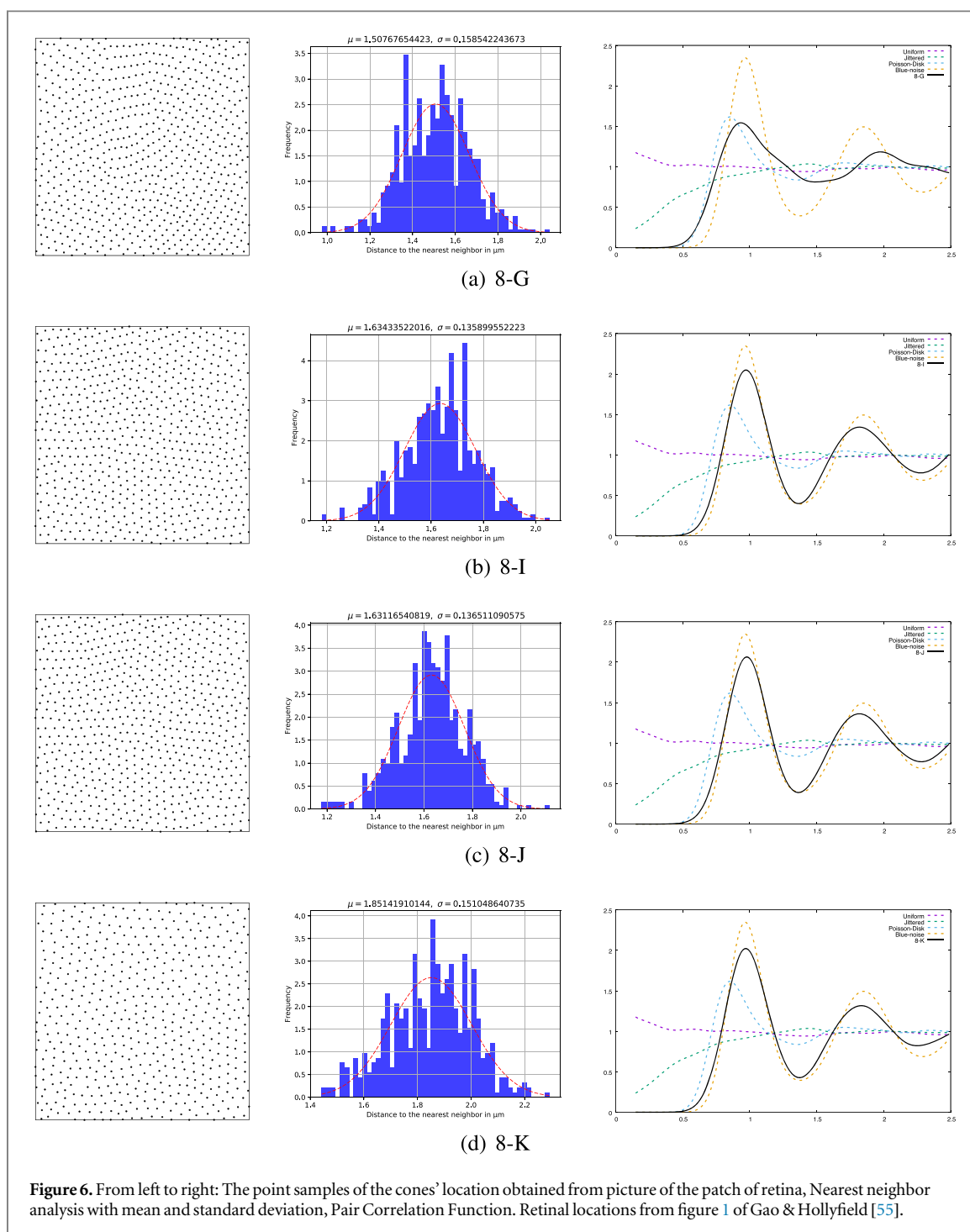
Figure 6. From left to right: The point samples of the cones' location obtained from picture of the patch of retina, Nearest neighbor analysis with mean and standard deviation, Pair Correlation Function. Retinal locations from figure 1 of Gao & Hollyfield [55].

whole retina is difficult to obtain and analyze. All validations should in fact be local. Future works will explore the possibility of applying a smooth sampling across the retina to obtain an adaptive sampling, given the PCF and spectra of local patches, the patches can be reproduced [67] and correlated with a heat map that represents interpolation in space [68].

6. Compliance with ethical standards

The authors declare that they have no conflict of interest. This reasearch does not involve human participants and/or animals. Informed consent is not appliable.

ORCID iDs

Matteo Paolo Lanaro ⓘ https://orcid.org/0000-0001-6191-4621

References

[1] Wassle H and Riemann H J 1978 The mosaic of nerve cells in the mammalian retina *Proc. of the Royal Society of London B: Biological Sciences* **200** 441–61

[2] Yellott J I 1983 Spectral consequences of photoreceptor sampling in the rhesus retina *Science* **221** 382–385

[3] Galli-Resta L, Novelli E, Kryger Z, Jacobs G H and Reese B E 1999 Modelling the mosaic organization of rod and cone photoreceptors with a minimal-spacing rule *European Journal of Neuroscience* **11** 1461–9

[4] Lagae A 2009 Wang tiles in computer graphics *Synthesis Lectures on Computer Graphics and Animation* **4** 1–91

[5] Dees E W, Dubra A and Baraas R C 2011 Variability in parafoveal cone mosaic in normal trichromatic individuals *Biomedical Optics Express* **2** 1351–8

[6] Hofer H, Singer B and Williams D R 2005 Different sensations from cones with the same photopigment *Journal of Vision* **5** 5–5

[7] Wohrer A and Kornprobst P 2009 Virtual retina: a biological retina model and simulator, with contrast gain control *J. Comput. Neurosci.* **26** 219–49

[8] Morillas C *et al* 2015 Towards a generic simulation tool of retina models *International Work-Conf. on the Interplay Between Natural and Artificial Computation* (Berlin: Springer) pp 47–57

[9] Morillas C *et al* 2017 A conductance-based neuronal network model for color coding in the primate foveal retina *International Work-Conf. on the Interplay Between Natural and Artificial Computation* (Switzerland: Springer) pp 63–74

[10] Ahumada A J Jr and Poirson A 1987 Cone sampling array models *J. Opt. Soc. Am.* A **4** 1493–502

[11] Curcio C A and Sloan K R 1992 Packing geometry of human cone photoreceptors: variation with eccentricity and evidence for local anisotropy *Visual neuroscience* **9** 169–80

[12] Wang Y-Z, Thibos L N and Bradley A 2001 Modeling the sampling properties of human cone photoreceptor mosaic *Vision Science and its Applications* (Washington, D.C.: Optical Society of America) p FB1

[13] Deering M F 2005 A human eye retinal cone synthesizer *ACM SIGGRAPH 2005 Sketches* (New York: ACM) p 128

[14] Curcio C A, Sloan K R, Kalina R E and Hendrickson A E 1990 Human photoreceptor topography *Journal of Comparative Neurology* **292** 497–523

[15] Ulichney R 1987 *Digital Halftoning* (Cambridge, MA: MIT Press) 9780262210096

[16] Floyd R W and Steinberg L 1976 An adaptive algorithm for spatial grey scale *Proc. Soc. Inf. Display* **17** 75–7

[17] Crow F C 1977 The aliasing problem in computer-generated shaded images *Commun. ACM* **20** 799–805

[18] Cook R L 1986 Stochastic sampling in computer graphics *ACM Trans. Graph.* **5** 51–72

[19] Mitchell D P 1987 Generating antialiased images at low sampling densities *ACM SIGGRAPH* **4** 65–72

[20] McCool M and Fiume E 1992 Hierarchical Poisson disk sampling distributions *Proc. Graphics Interface '92* pp 94–105

[21] Jones T R 2006 Efficient generation of Poisson-disk sampling patterns *Journal of Graphics, GPU, & Game Tools* **11** 27–36

[22] Bridson R 2007 Fast Poisson disk sampling in arbitrary dimensions *ACM SIGGRAPH Sketches* **10** 1278780–807

[23] Gamito M N and Maddock S C 2009 Accurate multidimensional Poisson-disk sampling *ACM Trans. Graph.* **29** 8:1–8:19

[24] Dunbar D and Humphreys G 2006 A spatial data structure for fast poisson-disk sample generation *ACM Trans. Graph.* **25** 503–8

[25] Ebeida M S, Davidson A A, Patney A, Knupp P M, Mitchell S A and Owens J D 2011 Efficient maximal Poisson-disk sampling *ACM Trans. Graph.* **30** 49:1–49:12

[26] Wei L-Y 2008 Parallel Poisson disk sampling *ACM Trans. Graph. (SIGGRAPH)* **27** 20:1–20:9

[27] Bowers J, Wang R, Wei L-Y and Maletz D 2010 Parallel Poisson disk sampling with spectrum analysis on surfaces *ACM Trans. Graph.* **29** 166:1–166:10

[28] Xiang Y, Xin S-Q, Sun Q and He Y 2011 Parallel and accurate Poisson disk sampling on arbitrary surfaces *SIGGRAPH Asia Sketches* **18** 1–2

[29] Dippé M A Z and Wold E H 1985 Antialiasing through stochastic sampling *ACM SIGGRAPH Proceedings of the 12th annual conference on Computer graphics and interactive techniques* **1** 69–78

[30] Mitchell D P 1991 Spectrally optimal sampling for distributed ray tracing *Proc. SIGGRAPH '91* vol 25, pp 157–64

[31] Shirley P S 1991 Discrepancy as a quality measure for sample distributions *Proc. Eurographics '91* pp 183–94

[32] Lagae A and Dutré P 2008 A comparison of methods for generating poisson disk distributions *Comput. Graphics Forum* **27** 114–29

[33] Balzer M, Schlömer T and Deussen O 2009 Capacity-constrained point distributions: a variant of Lloyd's method *ACM Trans. Graph.* **28** 86:1–8

[34] Ebeida M S, Mitchell S A, Patney A, Davidson A A and Owens J D 2012 A simple algorithm for maximal poisson-disk sampling in high dimensions *Comp. Graph. Forum* **31** 785–94

[35] Chen Z, Yuan Z, Choi Y-K, Liu L and Wang W 2012 Variational blue noise sampling *IEEE Trans. Visual Comput. Graphics* **18** 1784–96

[36] Schmaltz C, Gwosdek P, Bruhn A and Weickert J 2010 Electrostatic halftoning *Comput. Graph. Forum* **29** 2313–27

[37] Schlömer T, Heck D and Deussen O 2011 Farthest-point optimized point sets with maximized minimum distance *Symp. on High Performance Graphics* pp 135–42

[38] Fattal R 2011 Blue-noise point sampling using kernel density model *ACM Trans. Graph.* **30** 48:1–48:12

[39] de Goes F, Breeden K, Ostromoukhov V and Desbrun M 2012 Blue noise through optimal transport *ACM Trans. Graph.* **31** 171:1–171:11

[40] Zhou Y, Huang H, Wei L-Y and Wang R 2012 Point sampling with general noise spectrum *ACM Trans. Graph.* **31** 76:1–76:11

[41] Öztireli A C and Gross M 2012 Analysis and synthesis of point distributions based on pair correlation *ACM Trans. Graph. (Proc. of ACM SIGGRAPH ASIA)* **31** 1–10

[42] Heck D, Schlömer T and Deussen O 2013 Blue noise sampling with controlled aliasing *ACM Trans. Graph.* **32** 25:1–25:12

[43] Reinert B, Ritschel T, Seidel H-P and Georgiev I 2016 Projective blue-noise sampling *Comput. Graphics Forum* **35** 285–95

[44] Ostromoukhov V, Donohue C and Jodoin P-M 2004 Fast hierarchical importance sampling with blue noise properties *ACM Trans. Graph.* **23** 488–95

[45] Kopf J, Cohen-Or D, Deussen O and Lischinski D 2006 Recursive Wang tiles for real-time blue noise *ACM Trans. Graph.* **25** 509–18

[46] Ostromoukhov V 2007 Sampling with polyominoes *ACM Trans. Graph.* **26** 78:1–78:6

[47] Wachtel F, Pilleboue A, Coeurjolly D, Breeden K, Singh G, Cathelin G, de Goes F, Desbrun M and Ostromoukhov V 2014 Fast tile-based adaptive sampling with user-specified Fourier spectra *ACM Trans. Graph.* **33** 1-11

[48] Ahmed A, Perrier H, Coeurjolly D, Ostromoukhov V, Guo J, Yan H H D and Deussen O 2016 Low-discrepancy blue noise sampling *ACM Transactions on Graphics (Proc. of ACM SIGGRAPH Asia 2016)* **35** 247:1–247:13

[49] Ahmed A, Niese T, Huang H and Deussen O 2017 An adaptive point sampler on a regular lattice *ACM Trans. Graph.* **36** 138:1–138:13

[50] Cohen M F, Shade J, Hiller S and Deussen O 2003 Wang tiles for image and texture generation *ACM SIGGRAPH* **3** 287–94

[51] Lagae A and Dutré P 2006 An Alternative for Wang Tiles: Colored Edges versus Colored Corners *ACM Trans. Graph.* **25** 1442–59

[52] Ahmed A G M, Huang H and Deussen O 2015 Aa patterns for point sets with controlled spectral properties *ACM Transactions on Graphics (TOG)* **34** 212

[53] Jonas J B, Schneider U and Naumann G O H 1992 Count and density of human retinal photoreceptors *Graefe's Archive for Clinical and Experimental Ophthalmology* **230** 505–10

[54] Curcio C A, Allen K A, Sloan K R, Lerea C L, Hurley J B, Klock I B and Milam A H 1991 Distribution and morphology of human cone photoreceptors stained with anti-blue opsin *Journal of Comparative Neurology* **312** 610–24

[55] Gao H and Hollyfield J G 1992 Aging of the human retina. differential loss of neurons and retinal pigment epithelial cells *Investigative Ophthalmol. Vis. Sci.* **33** 1–17

[56] Roorda A and Williams D R 1999 The arrangement of the three cone classes in the living human eye *Nature* **397** 520–2

[57] Song H, Chui T Y P, Zhong Z, Elsner A E and Burns S A 2011 Variation of cone photoreceptor packing density with retinal eccentricity and age *Investigative Ophthalmol. Vis. Sci.* **52** 7376–84

[58] Scoles D, Sulai Y N, Langlo C S, Fishman G A, Curcio C A, Carroll J and Dubra A 2014 *In vivo* imaging of human cone photoreceptor inner segmentsin vivo imaging of photoreceptor inner segments *Investigative Ophthalmol. Vis. Sci.* **55** 4244–51

[59] Wong K S K, Jian Y, Cua M, Bonora S, Zawadzki R J and Sarunic M V 2015 *In vivo* imaging of human photoreceptor mosaic with wavefront sensorless adaptive optics optical coherence tomography *Biomedical Optics Express* **6** 580–90

[60] Rohatgi A 2017 Webplotdigitizer (http://arohatgi.info/WebPlotDigitizer/app)

[61] Drasdo N and Fowler C W 1974 Non-linear projection of the retinal image in a wide-angle schematic eye *The British journal of ophthalmology* **58** 709

[62] Wyszecki G and Stiles W S 1982 *Color science. Concepts and Methods, Quantitative Data and Formulae, 2nd Edition* vol 8 (New York: Wiley) 978-0-471-39918-6

[63] Illian J, Penttinen A, Stoyan H and Stoyan D 2008 *Statistical Analysis and Modelling of Spatial Point Patterns* vol 70 (New York: Wiley) 978-0470014912

[64] Gamito M N and Maddock S C 2009 Accurate multidimensional poisson-disk sampling *ACM Transactions on Graphics (TOG)* **29** 8

[65] Eglen S J 2012 Cellular spacing: analysis and modelling of retinal mosaics *Computational Systems Neurobiology* (Berlin: Springer) pp 365–85

[66] Cook J E 1996 Spatial properties of retinal mosaics: an empirical evaluation of some existing measures *Visual neuroscience* **13** 15–30

[67] Zhou Y, Huang H, Wei L-Y and Wang R 2012 Point sampling with general noise spectrum *ACM Transactions on Graphics (TOG)* **31** 76

[68] Roveri R, Öztireli A C and Gross M 2017 General point sampling with adaptive density and correlations *Comput. Graphics Forum* **36** 107–17 Wiley Online Library